

# Ultrasonic motor-induced geometric distortions in magnetic resonance images

P. Shokrollahi<sup>1,2</sup> · J. M. Drake<sup>1,2</sup> · A. A. Goldenberg<sup>1,3</sup>

Received: 30 December 2016 / Accepted: 10 June 2017 / Published online: 3 July 2017  
© International Federation for Medical and Biological Engineering 2017

**Abstract** Ultrasonic motors (USMs) are common actuators that can be safely used in the magnetic resonance imaging (MRI) environment. However, lack of MRI compatibility results in issues such as image distortion. This fact led researchers to shift focus from USMs to pneumatic and hydraulic actuators in development of surgical robots. The aim is to quantify and compensate the geometric distortion of MR images as generated by the presence of USMs. An ultrasonic motor was positioned in three orientations with respect to the bore axis. The induced distortions were compared across four image sequences. To reduce the distortions, three artifact reduction methods were employed. Geometric distortion is the only artifact in image slices farther from the motor. The various motor orientations lead to different distortions, with the lowest distortion for the  $z$  orientation. The maximum measured distortion of ten pixels occurred. This maximal distortion is equal to a 1-cm displacement of the displayed points relative to their actual locations and it is beyond the acceptable level for medical display standards. Bandwidth reduction reduced the distortion, with a 50% reduction for a doubled bandwidth. In conclusion, USMs can be preferred alternative

because accurate targeting of pathologies can occur in free distorted images.

**Keywords** MRI-compatibility · Ultrasonic motor · Geometric distortion · Artifact reduction · Robotic surgery

## 1 Introduction

The outstanding capabilities of MRI for localization and robots for targeting pathologies can provide more possibilities for computational methods and MRI-guided interventions. The numerous advantages of imaging techniques can be combined with those of manipulator mechanisms. Practitioners will be able to perform more complicated and varied types of procedures. Surgical instruments can be tracked in real time, and the issue of tissue deflection during operations can be solved. The spatial constraints of high-resolution closed-bore MRI systems will be overcome by the development of robotic manipulators and sensors for surgical instrumentation [1]. However, these features require the development of a new generation of actuators that have high accuracy, great efficiency, and compatibility with MRI.

MRI is considered the best modality for detecting tumors [2]. Its excellent soft-tissue contrast avoids trauma to critical structures and facilitates tumor removal without ionizing radiation [3]. MRI has several advantages, including providing high-resolution, digitized 3D images, and a well-defined coordinate system. It is an ideal modality for real-time image-guided interventions because it provides precise, updated, and spatial information about the target tissue at any orientation with the ability to rapidly acquire a sequence of images [1].

Due to the ultrahigh magnetic field (3 Tesla and above), MRI imposes various limitations on the tools and materials that can be used. The field impedes the precise control of

---

✉ P. Shokrollahi  
peyman.shokrollahi@mail.utoronto.ca

<sup>1</sup> Institute of Biomaterials and Biomedical Engineering, University of Toronto, Rosebrugh Building, 164 College Street, Room 407, Toronto, ON M5S3G9, Canada

<sup>2</sup> Division of Neurosurgery, The Hospital for Sick Children, 555 University Avenue, Room 1504, Toronto, ON M5G1X8, Canada

<sup>3</sup> Department of Mechanical and Industrial Engineering, University of Toronto, 5 King's College Road, Room 106, Toronto, ON M5S3G8, Canada

electromechanical movements [4]. Conventional robotics cannot be applied in the magnetic resonance (MR) environment, nor can ferromagnetic materials due to the high magnetic attraction forces and heat. These materials and tools generate detrimental imaging artifacts when they are placed in close proximity to the imager, and they may cause robot signal distortions [2]. These artifacts are sufficient to degrade the image quality, thus limiting the use in therapeutic medicine. Avoiding the interference between these tools and the MRI system is a difficult task, especially when the system is in active motion.

Additionally, few “off-the-shelf” actuators are available that can be safely used in the vicinity of an MRI instrument without an effect on their operation or degradation of the image quality [4].

The above-mentioned reasons limit the type of actuators that can be utilized in the vicinity of the scanner to four types: ultrasonic, hydraulic, pneumatic, and remote-manual actuators [5]. Hydraulic systems are incompatible due to the risk of leakage in the highly restricted area of the operation room, which requires sterility [2]. Pneumatic systems are decoupled from electromagnetism and thus do not affect MR images; however, they lack precise controllability, have a slow response time, and require a brake to stop the system in emergency conditions. Remote-manual actuators have lengthy procedures. Currently, patients must be removed from the scanner; then, the preoperative image is used as a roadmap to generate and place fiducial markers. Thereafter, the patient must be rescanned to validate the marker locations [6]. When MR contrast agents are employed, a lengthy procedure is an issue because the agents that are used to identify lesions have a short lifetime of 10 min [7].

Even though pneumatic and hydraulic systems address a few of these compatibility issues, they cannot provide the numerous advantages of ultrasonic motors (USMs). USMs are the most promising actuators despite the fact that they may interfere with the scanner. The small size of USMs overcomes the patient accessibility issues of cylindrical, closed-bore MRI systems. USMs also have the advantage of precise controllability, a high torque/size ratio, a short response time, and instant stopping by powering off the motor. Unlike electromagnetic motors, USMs are not driven by magnetism. Instead, USMs operate based on the vibrational modes generated in the piezoelectric materials of the stator; traveling waves produced in the stator move the rotor located on the top through frictional forces [8].

USMs can be utilized as effective actuators to perform surgeries safely with high precision and full controllability. However, USMs interact with MRI systems and they distort MR images. To address compatibility issues, USMs were kept at a distance (at least 50 cm) from an MR scanner [6]. Therefore, the behavior of USMs in MRI systems must be enhanced to provide engineering solutions to improve the design of these actuators, reduce their interactions, and achieve

the desired level of MRI compatibility and image quality [4]. The strong capabilities of USMs can be retained and enhancements can be made to address USMs’ compatibility issues. This can lead to safer operation of USMs in high field MRI and enable practitioners to accurately and safely operate surgical tools.

The aim of this research is to quantify and compensate the geometric distortion of MR images as generated by the presence of USMs. The problem considered in this study is as follows: the presence of the USM induces a geometrical distortion in MR images that causes the displacement of the displayed points relative to their actual locations and improper scaling of the distance between any points within the image. These displacements result in the misplacement of an actuated needle or drill in tissue and reduces the accuracy of the robot.

## 2 Methods

The internal and external magnetic flux densities are calculated inside and outside a sphere respectively within a homogeneous field by using Laplace’s equation and by applying boundary conditions [9]. The shift from the ideal to actual excited slices ( $\Delta y$ ) can be calculated from these equations inside ( $\Delta y_i$ ) and outside ( $\Delta y_e$ ) the sphere as follows:

$$y_i = \frac{2}{3} \Delta\chi \frac{B_0}{G_y}, \quad y \leq R \quad (1a)$$

$$\Delta y_e = \frac{\Delta\chi}{3} \frac{B_0}{G_y} R^3 \frac{2z^2 - x^2 - y^2}{(x^2 + y^2 + z^2)^{5/2}}, \quad y \geq R \quad (1b)$$

where  $\Delta\chi = \mu_e - \mu_i$  ( $\mu_e$  and  $\mu_i$  are the external and internal relative permeabilities, respectively, of the spherical object),  $R$  is the sphere radius,  $B_0$  is the intensity of static field, and  $G_y$  is the magnitude of gradient field in the  $y$  direction. As Eq. 1b is an implicit equation, the maximum shift is calculated for  $|z| = R$  as follows [9]:

$$(\Delta y_e)_{\max} = \frac{\Delta\chi}{3} \frac{B_0}{G_y} \quad (2)$$

If the motor is modeled by an aluminum or brass sphere of 45 mm diameter, the maximum slice shift can be calculated using Eq. 2, as follows:

$$B_0 = 3 \text{ T}, \quad G_y = 40 \frac{mT}{m};$$

Inner material: for aluminum,  $\chi_i = 2.2 \times 10^{-5}$  and for brass,  $\chi_i = 2.2 \times 10^{-4}$

Outer material (air):  $\chi_e = 0$ ;

$|\Delta y_e|_{\max}$  is 1.1 and 11 mm for aluminum and brass, respectively.

Linear distortion can be characterized by measuring the curvature of distortion. A reference image is obtained with a profile similar to that of a chessboard, with equally spaced vertical and horizontal lines. For this purpose, a grid phantom was designed and implemented to cover the maximum possible field of view. The phantom was placed within a 32-channel Philips head coil (Philips Healthcare, Best, the Netherlands); it was large enough to evaluate all image artifacts induced by the motor, and it had equally spaced horizontal and vertical lines for the grids [10]. The structure had a cylindrical form (Fig. 1) with the following characteristics: height of 15 cm, outer/inner diameters of 12.5/11.5 cm, bottom thickness of 5 mm, grid type of square with 2-cm sides, gap between the grids of 2 mm, lid thickness of 5 mm, and material of Nylon 12.

The largest distortion ( $l$ ) was computed by calculating the distance between the farthest point on the line on the distorted image and the corresponding point on the reference image. The distortion was described as the  $l/L$  ratio in percentage, where  $L$  is the length of the undistorted line [11]. To quantify the distortion,  $l$  and the root mean square (RMS) values of the distances between the reference and distorted points were used in this article.

The reference images were obtained by imaging the phantom in the absence of the motor. These images were compared with the images of the phantom when the motor was present. Three motor orientations ( $x$ ,  $y$ , and  $z$ ) exist with respect to the bore: the  $x$  orientation is when the motor shaft is parallel to the patient table and perpendicular to the bore axis, the  $y$  orientation is when the motor shaft is perpendicular to the patient table, and the  $z$  orientation is when the shaft is parallel to the bore axis. Two motor states (on and off) were evaluated. The geometric distortions of the grids were visually assessed by comparing the distorted images and their corresponding reference images.

## 2.1 Image specifications

A 3.0 Tesla scanner (Achieva, Philips Medical Systems, Best, the Netherlands) was used, and the phantom was placed in the 32-channel head coil (Philips) to receive full-strength signals.

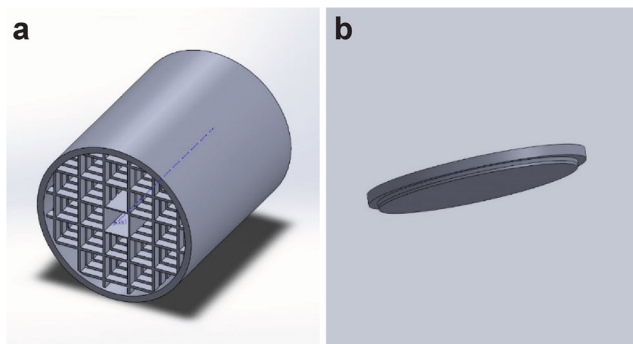


**Fig. 1** **a** The grid phantom, **b** the phantom lid

Conventional clinical pulse sequences, including T1-weighted spin echo (T1W) and T2-weighted turbo spin echo (T2W), were employed in two orientations, transverse (axial) and coronal (parallel to the patient bed). The scan parameters were as follows:

- T1W: echo time (TE) = 10 ms, repetition time (TR) = 0.60 s, field of view (FOV) =  $125 \times 125 \times 125$  mm, in-plane voxel size = 1 mm, slice thickness = 5 mm, and flip angle =  $70^\circ$ .
- T2W: TE = 80 ms, TR = 3 s, FOV =  $125 \times 125 \times 135$  mm, in-plane voxel size = 1 mm, slice thickness = 5 mm, flip angle =  $90^\circ$ .

## 2.2 Distortion measurement

Two types of algorithms were developed using MATLAB 2013b to detect and calculate the geometric distortions. In both algorithms, the horizontal lines of the distorted images were detected and compared with their corresponding reference lines for all motor configurations.

### 2.2.1 Thresholding algorithm

This algorithm was based on a threshold value of the image intensity that was used to detect the grid lines. Various thresholding values were tested to find the optimum one. After the image was segmented, the horizontal lines were extracted, and the distorted lines were compared with their reference to find the RMS and maximum distortion. The thresholding algorithm was as follows:

```

Start
For (slice selection)
  For (configuration selection)
    Image Thresholding
    Image Segmentation
    Line Extraction
    Noise Reduction
    RMS Distortion Calculation
    Max Distortion Calculation
  End
End
End
End

```

### 2.2.2 Edge detection algorithm

To overcome the difficulty of thresholding and avoid the detection of other artifacts (e.g., signal pileups), an edge detection algorithm was developed in MATLAB. This algorithm

was based on the detection of the edges of horizontal lines, the selection of an upper edge or lower edge, and a calculation of the distortion (Fig. 2). In this method, the distortion was calculated as the vertical distance between the maximum and minimum of the selected points of the distorted line. The distortion was assumed to be nonsignificant at both ends of the

detected edge; therefore, the edge points were mostly assumed to be the minimum points and used as the reference (Fig. 2). However, this algorithm has the limitation of incorrect edge detection. Thus, the detected edge in each image was visually plotted and validated. The edge detection algorithm is as follows:

*Start*

*Image Selection (i.e., sequence and slice selection)*

*Image Importation*

*Image Segmentation (i.e., segmentation of the circular region of the phantom)*

*Edge Detection (i.e., detection of the upper/lower edge of the horizontal grid lines)*

*Image Exportation (including the detected edges for verification)*

*Max Distortion Calculation*

*End*

## 2.3 Compensation methods

### 2.3.1 Compensating by developing the mapping transformation matrix

Two approaches can be used to reduce geometric distortion: one at the source (motor) and one at the target (image). The solution at the source includes improving the motor design, encoder type, and shielding structure or designing a new MRI receiver coil specifically for

the motor, whereas the solution at the target includes software development. A solution at the source can remove all types of motor-induced artifacts, including geometric distortions. The solution at the target is preferred when a geometric distortion is involved for the following reasons:

- Easy to control the MR sequence specifications
- Easy to develop a program to compensate for distortion, e.g., using MATLAB
- Well-established and well-known conventional image processing solutions have previously been used to address the problem
- Much more effective solution and less complexity is involved

One approach for removing geometric distortion is to develop a transformation matrix to map the distorted points of the image back to their proper locations. We have developed a transformation matrix using MATLAB for one distorted line in the image of the grid phantom. A comprehensive transformation could be derived by expanding the algorithm to all grid lines by combining the transformations of each individual line for each slice. However, the complexity of such an algorithm is high, leading to an increase in the scan time. Additionally, providing the matrix with an accepted clinical standard requires a large number of tissue imaging experiments. Additionally, the images sometimes include other types of artifacts besides geometric distortion, and fixing the geometric distortion would be useless without removing the other artifacts. Additionally, this method is feasible,

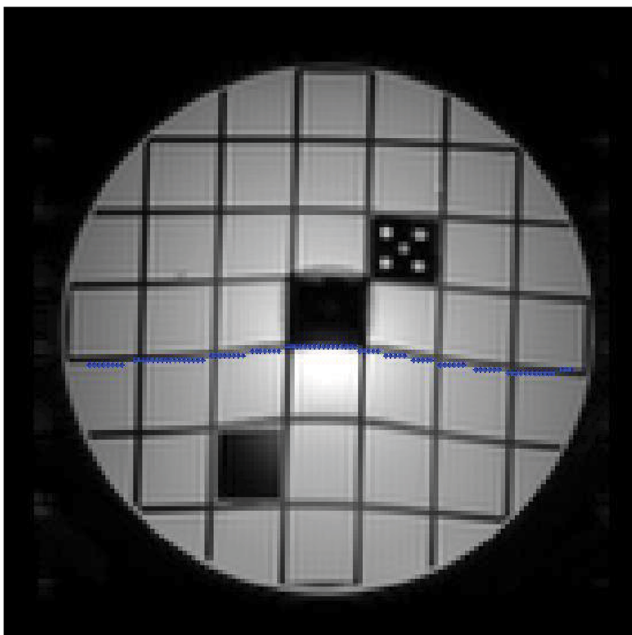


**Fig. 2** Detecting the lower edge of the horizontal grid using the edge detection algorithm

and many compensation methods can be adopted from established image processing methods, which are referred to as “unwarping” [12]. Developing such an algorithm requires knowledge of other facts, such as the complexity of the distorted image due to SNR degradation when the motor is present, and requires minimizing the time needed for image post processing to save clinical time and facilitate real-time interventions.

### 2.3.2 Compensation through control of the pulse sequences

Three artifact reduction methods were employed: sequence selection, slice thickness reductions, and bandwidth increments [13, 14]. To understand the effect of these factors on the geometric distortions, geometric distortions were quantified using four sequences (T1W, T2W, turbo spin echo (TSE), and fast field echo (FFE) with the following properties:

- T1W: TE = 10 ms, TR = 0.60 s, FOV = 160 × 160 × 150 mm, in-plane voxel size = 1 mm, slice thickness = 5 mm, and flip angle = 70°.
- T2W: TE = 80 ms, TR = 3 s, FOV = 160 × 160 × 150 mm, in-plane voxel size = 1 mm, slice thickness = 5 mm, flip angle = 90°.
- TSE: TE = 72 ms, TR = 4 s, FOV = 160 × 160 × 150 mm, in-plane voxel size = 1 mm, slice thickness = 5 mm, flip angle = 90°.
- FFE: TE = 2.8 ms, TR = 12.1 ms, FOV = 160 × 160 × 150 mm, in-plane voxel size = 1 mm, slice thickness = 5 mm, and flip angle = 30°.

The same parameters were used to compare the effects of the sequences. These sequence parameters included the slice thickness, BW, number of signals averaged (NSA; =1), and turbo factor (=1). The effects of TH reduction and BW increments were compared. For the  $y$  orientation of the motor, three slice thicknesses (5, 3, and 1 mm) with two BWs (437 and 875 Hz) were tested.

In this comparison, the distortion ratios were measured using a DICOM viewer (RadiAnt DICOM Viewer, version 2.2.9; Meixant, Poznan, Poland) for images that were collected with the minimum and maximum bandwidth and for the three slice thicknesses, 5, 3, and 1 mm.

## 3 Results

Geometric distortions were observed in all motor orientations. Figure 3 shows three orientations of the motor in the MRI scanner. The distortion was less when the motor was in the  $z$  orientation was greater when the motor was in the  $x$  or  $y$  orientation. The geometric distortion of the powered motor (“on”) was not detectable. The motor was tested at three

speeds: 25, 75, and 95% of the maximum speed. However, nonsignificant distortions were observed in all cases.

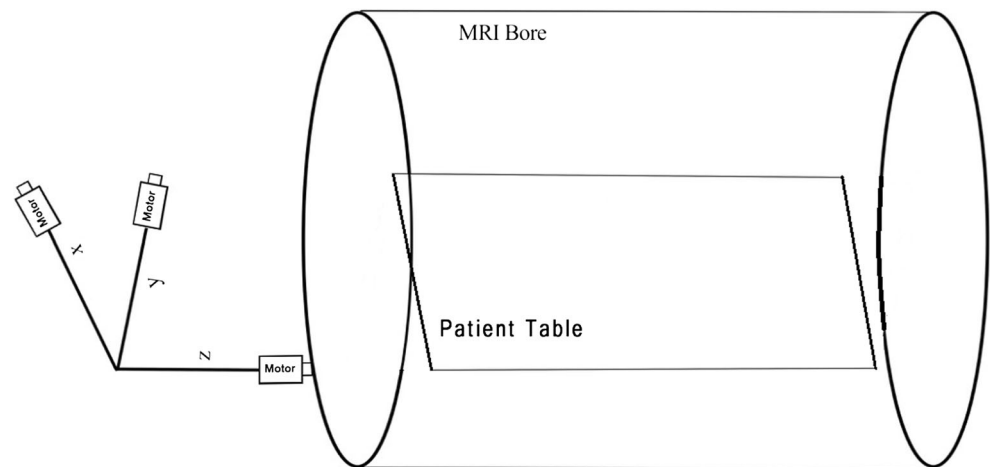
The thresholding algorithm was applied, as shown in Fig. 4, to the third slice of the T1W transverse image of the reference (a) and the corresponding selected center line of the grid (b). The figure compares all configurations ( $y$  (c),  $z$  (e), and  $x$  (g)) with their corresponding center lines (b, d, f, and h) in the “off” state. Figure 4 (g) shows the geometric distortion when the motor was “on.” Although the zipper artifacts appear in the image when the motor is on, the geometric distortion remains unaffected. The center line, along with one line above and one line below the center, was considered in this algorithm because of the significant distortions compared with those of the other lines.

The RMS and maximum distortion were measured in pixels. The maximum distortion was defined as the maximum distance (in pixels) between the corresponding points on the reference and distorted lines. The distortion is greater when an image slice is closer to the motor. However, in image slices that are very close to the motor, image artifacts other than geometric distortion, such as signal voids, may be present. Figure 5 illustrates the root mean square (RMS) and maximum distortion (max dist) values calculated for T1- and T2-weighted sequences for transverse images of the third slice. The values are for three horizontal lines of the phantom: the center line (line 0), one line above the center line (line +1), and one line below the center line (line -1). The  $x$ ,  $y$ , and  $z$  orientations of the motor inside the bore are each represented. Figure 5 displays the distortion measurements for the third slice showing the maximum geometric distortion without the presence of signal voids. In the transverse images, the center of the phantom image was close to the motor. Consequently, greater distortion was observed and calculated for the three center lines of the phantom. Figure 6 illustrates the root mean square (RMS) and maximum distortion (max dist) values calculated for T1- and T2-weighted sequences for the coronal images of slices 8–10, which had the highest distortions of the grid phantom. The values are for two horizontal lines of the phantom: the bottom line (first line) and one line above the bottom line (second line). The  $x$ ,  $y$ , and  $z$  orientations of the motor inside the bore are each represented. Figure 6 displays the measurements for the images that are closer to the motor and have greater distortion than other slices. In the coronal images, the bottom of the phantom image was close to the motor. Thus, greater distortion was observed and calculated for the two bottom lines of the phantom.

### 3.1 Compensation of geometric distortions

Table 1 shows the distortion ratio for four sequences, three slice thicknesses, and two bandwidths. In the six tested

**Fig. 3** Three orientations of the motor in the MRI scanner



sequences, the selection of sequence did not affect the size of the geometric distortions. The reduction in slice thickness also did not affect the distortion size. However, the depth over

which the distortions were present was reduced by decreases in the slice thickness. Slice thickness reduction may result in SNR degradation. When TH reached 1 mm in the FFE

**Fig. 4** Geometric distortion of the motor orientations with the corresponding *center line* that was selected by the thresholding algorithm. The thresholding algorithm was applied to the third slice of the T1W transverse image of the reference (a) and the corresponding selected center line of the grid (b). The figure compares all configurations (y (c), z (e), and x (g)) with their corresponding *center lines* (d, f, and h)

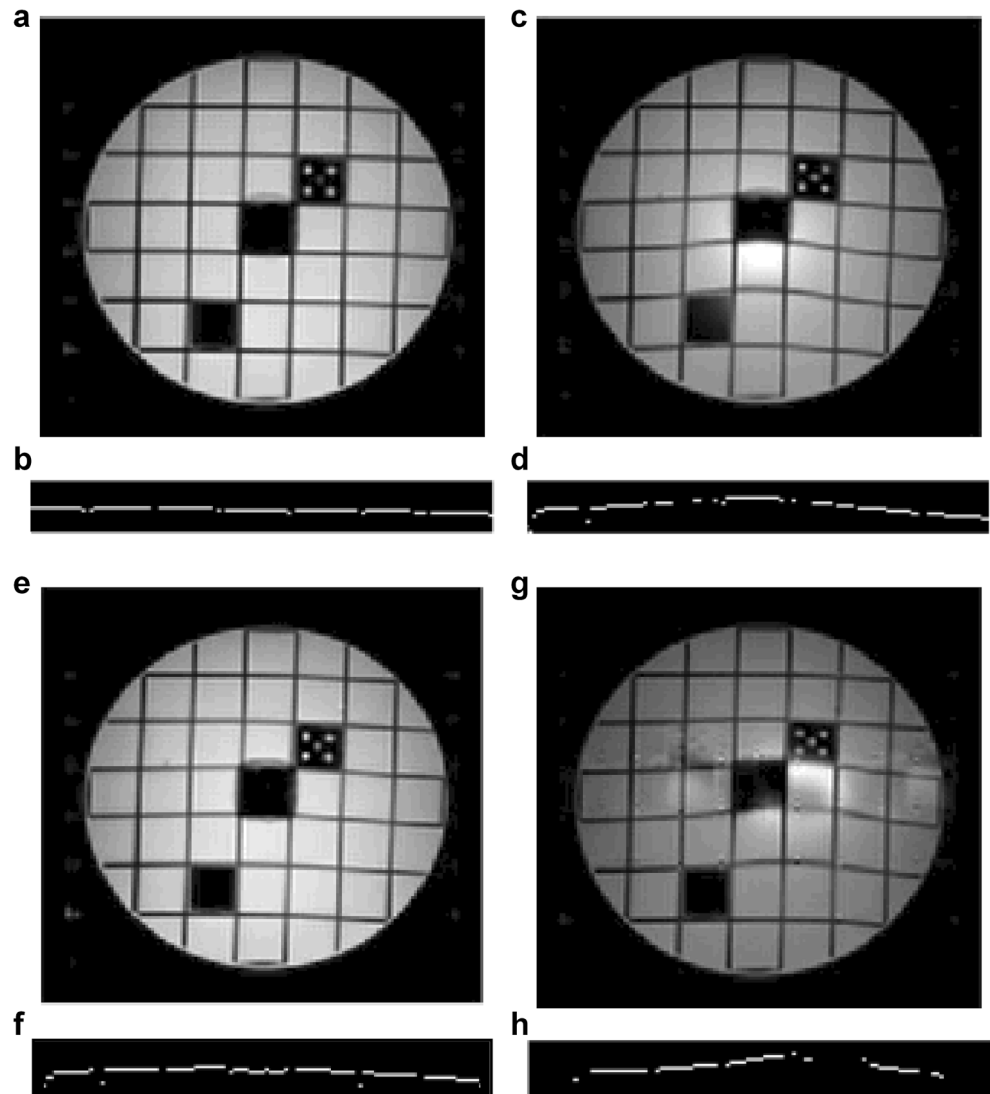
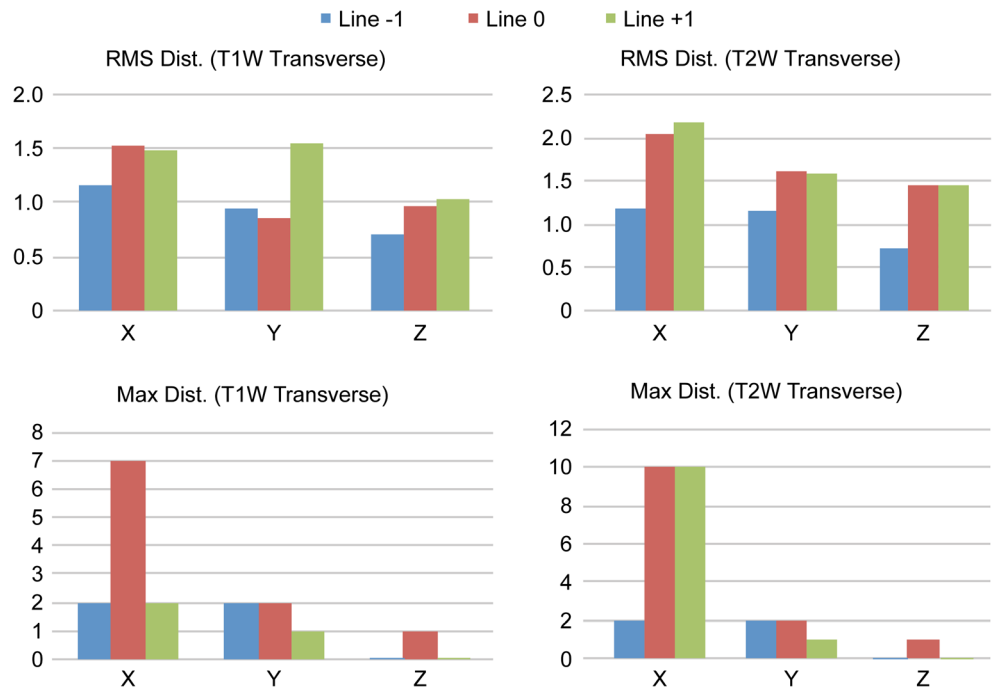


**Fig. 5** The root mean square (RMS) and maximum distortion (max dist) values for T1- and T2-weighted sequences for transverse images of the third slice. The values are for *three horizontal lines* of the phantom: the *center line* (line 0), one *line above the center line* (line +1), and one *line below the center line* (line -1). The *x*, *y*, and *z* orientations of the motor inside the bore are each represented



sequence, the SNR was too low to measure the geometric distortions. Bandwidth increments reduced the geometric distortions. Doubling the BW resulted in a 50% reduction in the distortion in most of the cases.

#### 4 Discussions

The degree of distortion is not uniform and varies with the radial distance between the imaging position and the motor location.

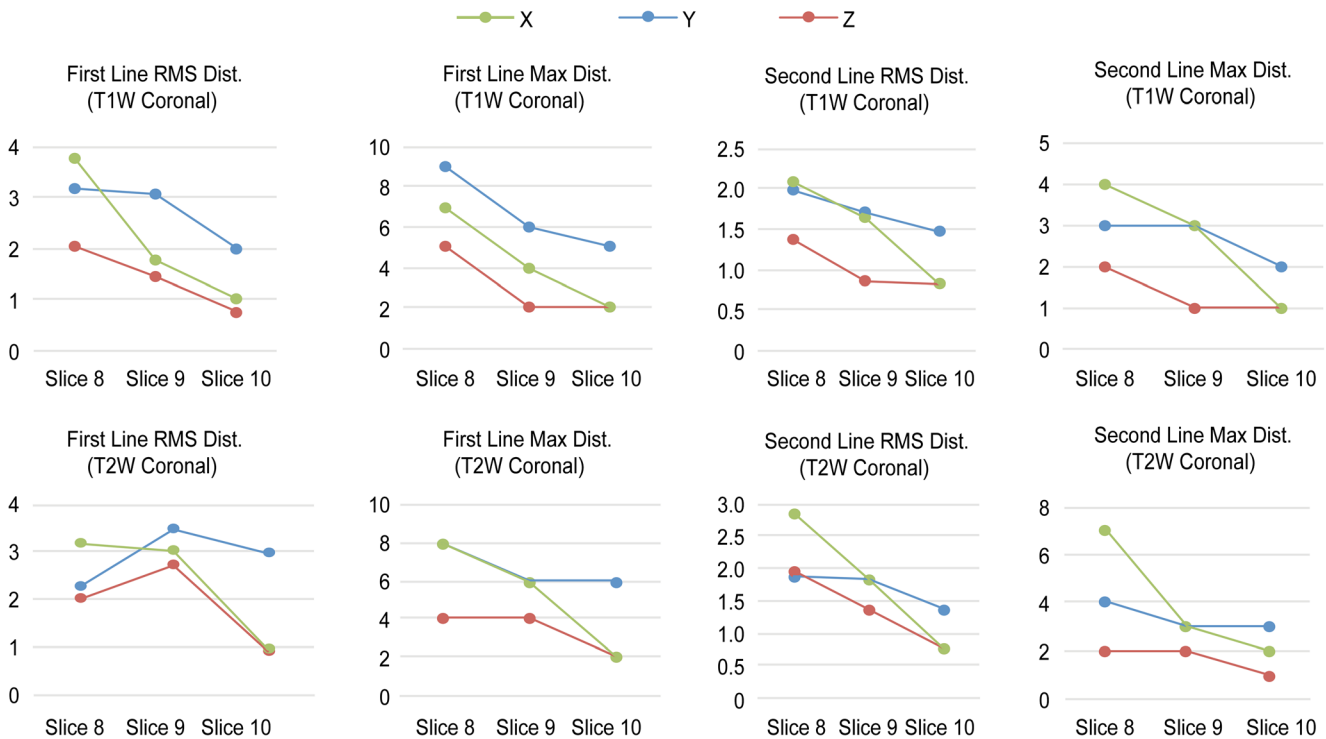


**Fig. 6** The root mean square (RMS) and maximum distortion (max dist) values calculated for T1- and T2-weighted sequences for the coronal images of slices 8–10, which had the highest distortions of the grid phantom. The values are for *two horizontal lines* of the phantom: the

*bottom line (first line)* and one *line above the bottom line (second line)*. The *x*, *y*, and *z* orientations of the motor inside the bore are each represented

**Table 1** BW impact on geometric distortion

Sequence	TH (mm)	Depth of geometric distortion (mm)	Min/Max BW				Distance range for geometric distortion	Scanning duration (min)
			Min BW		Max BW			
			Max distortion (%)	Min distortion (%)	Max distortion (%)	Min distortion (%)		
T1W	5		4%	0.7%	2.3%	0.9%		1:57
		Distance from the motor	37	67	37	67	30	
	3		5.5%	1.7%	2.9%	1.1%		3:15
		Distance from the motor	34	58	34	58	24	
	1		3.7%	1.7%	2.9%	1.5%		9:45
		Distance from the motor	28	44	28	44	16	
T2W	5		4.9%	1.5%	2.1%	1.3%		1:06
		Distance from the motor	42	57	42	57	15	
	3		5.2%	1.8%	2.3%	0.9%		1:39
		Distance from the motor	34	46	34	46	12	
	1		6%	1.8%	2%	1.1%		4:57
		Distance from the Motor	27	45	27	45	18	
TSE	5		4.3%	1.4%	2.2%	0.9%		2:24
		Distance from the motor	37	57	37	57	20	
	3		4.3%	1.7%	2%	1.4%		3:12
		Distance from the motor	31	49	31	49	18	
	1		2.5%	2.3%	2%	1.5%		9:36
		Distance from the motor	34	39	34	39	5	
FFE	5		3.5%	1.3%	1.5%	0.9%		0:58
		Distance from the motor	27	58	27	58	31	
	3		3.1%	2%	1.5%	1.2%		1:33
		Distance from the motor	26	48	26	48	22	
	1		A low SNR hindered the measurement of the geometric distortion at this thickness					4:04

However, distortion can be approximated linearly. Distortion occurs in the phase-encoding direction due to the dephasing of spins. Because the motor shifted the frequency of spins to higher values in the frequency-encoding direction, upward distortion was observed in the images (refer to Fig. 2). The presence of distortions is due to the static field inhomogeneity caused by the metallic parts used in the motor case, stator ring, and encoder. The observed geometric distortions were found only in the frequency-encoding direction [15].

Distortion was minimal when the motor was in the  $z$  orientation. In this case, the motor was located in a symmetrical configuration with respect to the MRI fields. Therefore, the distortion of the field lines was less than that of the other configurations. Conversely, the other orientations showed material distortion due to nonsymmetrical orientation of the motor with respect to the magnetic fields, resulting in the appearance of substantial geometrical distortion.

The vertical distance between the grids was 2 cm, corresponding to 20 pixels in the MR image. Therefore, the maximum error caused by distortion would be ten pixels with a tolerance of one pixel, corresponding to a 1-cm error at a

distance of 2.5 cm from the motor. This error is significant, especially when targeting a sample using a needle/drill during surgical intervention. Moreover, this value causes a distortion ratio of 8.5%, which is beyond the acceptable level of 5% for medical display distortion [10]. The theoretical value for geometric distortion in the  $y$  direction is 1.1 and 11 mm for aluminum and brass, respectively. The experimental value of 1 cm is found to be consistent with the theoretical value. One of the reasons for the theoretical value being slightly lower than the experimental value is the assumptions in writing the formula. Bandwidth was assumed to be zero so that the slice thickness becomes zero. However, in reality, the slice thickness cannot be zero.

The desired spatial accuracy for geometric distortions is at least 2% [10]. The distortion level is enhanced to approximately two pixels by maximizing the bandwidth (Table 1), corresponding to a distortion ratio of 1.7% on average, which is equal to a 2-mm error in locating a position in the true dimension. This value is within the acceptable level for a medical display distortion. Therefore, the motor can safely and precisely operate approximately 6 cm away of isocenter.



## 5 Conclusion

Geometric distortion appears in slices close to the motor. Using two developed algorithms (thresholding and edge detection), the maximum distortion was evaluated to be ten pixels, which corresponds to a distortion ratio of 8.5% and beyond the acceptable level of 5% for a medical display distortion. Safer USM operation in the high-field MR environment can be achieved by minimizing geometric distortion. Doubling the BW resulted in a 50% reduction in the distortion. The distortion level is enhanced to approximately two pixels by maximizing the bandwidth. This value is within the acceptable level for a medical display distortion. These findings are theoretically and practically important because it is not necessary to keep the USMs at a distance from the MR scanner to address compatibility issues, as recommended in most research literatures to mitigate USM compatibility issues. Therefore, the USMs can be preferred alternative because the USMs have high precision in controllability that play a magnificent role in actuating MRI-compatible surgical robots and because accurate targeting of pathologies can occur in free distorted images.

**Acknowledgments** This work was financially supported by NSERC CHRP Grant 385860-10 to A. A. Goldenberg. Additionally, we thank Adam Waspe for his support.

## References

- Elhawary H, Tse ZT, Hamed A, Rea M, Davies BL, Lampert MU (2008) The case for MR-compatible robotics: a review of the state of the art. *Int J Med Rob* 4:105–113. doi:10.1002/rcs.192
- Stoianovici D, Song D, Petrisor D, Ursu D, Mazilu D, Mutener M, Schar M, Patriciu A (2007) “MRI Stealth” robot for prostate interventions. *Minim Invasive Ther Allied Technol* 16:241–248. doi:10.1080/13645700701520735
- Koseki Y, Washio T, Chinzei K, Iseki H (2002) Endoscope manipulator for trans-nasal neurosurgery, optimized for and compatible to vertical field open MRI. In: Dohi T, Kikinis R (eds) *Medical image computing and computer-assisted intervention—MICCAI 2002*. Springer Verlag, Berlin, pp 114–121
- Cole GA, Harrington K, Su H, Camilo A, Pilitsis JG, Fischer GS (2014) Closed-loop actuated surgical system utilizing real-time in-situ MRI guidance. In: Khatib O, Kumar V, Sukhatme G (eds) *Experimental robotics*. Springer Verlag, Berlin, pp 785–798
- Shokrollahi P, Drake JM, Goldenberg AA (2015) Comparing the effects of three MRI RF sequences on ultrasonic motors. In: Jaffray DA (ed) *World Congress on Medical Physics and Biomedical Engineering*, June 7–12, 2015, Toronto, Canada. Springer Verlag International Publishing, Toronto, pp 846–849
- Tsekos NV, Khanicheh A, Christoforou E, Mavroidis C (2007) Magnetic resonance-compatible robotic and mechatronics systems for image-guided interventions and rehabilitation: a review study. *Annu Rev Biomed Eng* 9:351–387. doi:10.1146/annurev.bioeng.9.121806.160642
- Tsekos NV, Shudy J, Yacoub E, Tsekos PV, Koutlas IG (2001) Development of a robotic device for MRI-guided interventions in the breast. *Proceedings of the 2nd IEEE International Symposium on Bioinformatics and Bioengineering*. IEEE, Bethesda, MD, USA, pp 201–208.
- Kumada A (1985) A piezoelectric ultrasonic motor. *Jpn J Appl Phys* 24:739–741
- Lüdeke KM, Röschmann P, Tischler R (1985) Susceptibility artefacts in NMR imaging. *Magn Reson Imaging* 3:329–343. doi:10.1016/0730-725X(85)90397-2
- Samei E, Badano A, Chakraborty D, Compton K, Cornelius C, Corrigan K, Flynn MJ, Hemminger B, Hangiandreou N, Johnson J, Moxley-Stevens DM, Pavlicek W, Roehrig H, Rutz L, Shepard J, Uzenoff RA, Wang J, Willis CE, AAPM TG18 (2005) Assessment of display performance for medical imaging systems: executive summary of AAPM TG18 report. *Med Phys* 32:1205–1225
- Wang Q, Desai VN, Ngo YZ, Cheng WC, Pfefer J (2013) Towards standardized assessment of endoscope optical performance: geometric distortion. *Proceedings of the International Conference on Optical Instrument & Technology*, Beijing, p 904205
- Gholipour A, Kehtarnavaz N, Scherrer B, Warfield SK (2011) On the accuracy of unwarping techniques for the correction of susceptibility-induced geometric distortion in magnetic resonance Echo-planar images. *Conf Proc IEEE Eng Med Biol Soc* 2011: 6997–7000
- Dietrich O, Reiser MF, Schoenberg SO (2008) Artifacts in 3-T MRI: physical background and reduction strategies. *Eur J Radiol* 65:29–35. doi:10.1016/j.ejrad.2007.11.005
- Hargreaves BA, Worters PW, Pauly KB, Pauly JM, Koch KM, Gold GE (2011) Metal-induced artifacts in MRI. *AJR Am J Roentgenol* 197:547–555. doi:10.2214/AJR.11.7364
- Baldwin LN, Wachowicz K, Thomas SD, Rivest R, Fallone BG (2007) Characterization, prediction, and correction of geometric distortion in 3T MR images. *Med Phys* 34:388–399. doi:10.1118/1.2402331



**Peyman Shokrollahi** (S' 07) was born in Tehran, Iran. He received his bachelor in electrical and electronics engineering from Shiraz University, Shiraz, Iran in 2001, and masters of applied science in electrical and computer engineering from Ryerson University, Toronto, Ontario, Canada in 2009. From 2007 to 2009, he was collaborating with Sunnybrook Hospital on sleep data analysis for investigating the medications effect on sleep and developing software for detection

of eye movements on data recorded from patients during sleep. Since 2012, he is collaborating with the Hospital for Sick Children in Toronto in developing surgical robots for pediatric bone biopsies. His research mainly focused on developing MRI-compatible sensors and actuators. Mr. Shokrollahi is the member of International Society for Magnetic Resonance in Medicine (ISMRM) and IEEE Engineering in Medicine and Biology Society (EMBS).



**James M. Drake** was born in London, Ontario, Canada. He received the B.S.E. degree in aerospace and mechanical engineering from Princeton University, Princeton in 1974, the MBBCh degree in medicine from Royal College of Surgeons in Ireland in 1979, the MSc degree in magnetic resonance imaging from University of Toronto, Toronto, in 1987, and FRCS in neurosurgery from Royal College of Surgeons of Canada in 1987. Since 2003, he is the Division

Chief of Pediatric Neurosurgery at the Hospital for Sick Children in Toronto. He is a Professor in the Department of mechanical and Industrial engineering at the University of Toronto. He holds the Harold Hoffman Shoppers Drug Mart Chair. He is a Senior Associate Scientist in the Sickkids Research Institute, and leads the Centre of Image Guided Innovation and Therapeutic Intervention. He is also Co-Director of the Centre of Mathematical Medicine at the Fields Institute at the University of Toronto. Dr. Drake has over 230 peer reviewed publications. He was a recipient of major grants from CIHR/NSERC, and Brain Canada from 2013 for his research relate to hydrocephalus including the use of endoscopy, image guided surgery for brain tumors and epilepsy, and the management of complex spinal disorders.



**Andrew A. Goldenberg** (S'73–M'76–SM'87–F'96) received the B.A.Sc. and M.A.Sc. degrees from Technion–Israel Institute of Technology in 1969 and 1972, respectively, and the Ph.D. degree from the University of Toronto in 1976, all in electrical engineering. From 1975 to 1981, he was with SPAR Aerospace Ltd., where he was involved in the research on the first Space Shuttle Remote Manipulator System—the Canadarm. Since 1982, he has been a Professor of mechanical and industrial engineering at the University of Toronto. He is the Founder and President of Engineering Services Inc., and the Founder and President of Anviv Mechatronics Inc. He was on the Editorial Boards of the Journal of Robotics, Robotica, and Robotics. He has authored or coauthored more than 135 peer-reviewed journal papers, more than 360 conference proceedings papers, and 12 chapters in books, and holds more than 33 patents. He is currently involved in technology research and development including: mobile, modular, and medical surgery robots, smart materials, and expert systems. Dr. Goldenberg was an Editor of the IEEE TRANSACTIONS ON ROBOTICS AND AUTOMATION. He is a Fellow of the American Society of Mechanical Engineers, the Engineering Institute of Canada, and the Canadian Academy of Engineering.

He is the Founder and President of Engineering Services Inc., and the Founder and President of Anviv Mechatronics Inc. He was on the Editorial Boards of the Journal of Robotics, Robotica, and Robotics. He has authored or coauthored more than 135 peer-reviewed journal papers, more than 360 conference proceedings papers, and 12 chapters in books, and holds more than 33 patents. He is currently involved in technology research and development including: mobile, modular, and medical surgery robots, smart materials, and expert systems. Dr. Goldenberg was an Editor of the IEEE TRANSACTIONS ON ROBOTICS AND AUTOMATION. He is a Fellow of the American Society of Mechanical Engineers, the Engineering Institute of Canada, and the Canadian Academy of Engineering.